CCUS: 4013924

An Integrated Reservoir Simulation and Geomechanical Modeling of CO_2 Injection at the Wyoming Dry Fork CarbonSAFE Geologic Storage Complex

Tao Bai*[1], Ying Yu[1], Peng Li[2], Zunsheng Jiao[1], Matthew Johnson[1], Charles Nye[1], Jonathan McLaughlin[1], Scott Quillinan[1], 1. Center for Economic Geology Research, School of Energy Resources, University of Wyoming, 2. Department of Geology and Geophysics, University of Wyoming.

Abstract

The Wyoming CarbonSAFE project is located at the Powder River Basin (PRB) in northeast Wyoming, which aims to safely store over 50 million metric tons of CO_2 for a period of 30 years at three stacked reservoirs including Lakota sandstone, Hulett sandstone, and Upper Minnelusa formation. Site-specific characterization data, including well logs, seismic data, core data, and field tests, are integrated into the dynamic model for initializing reservoir pressure and regional stress state and estimating petrophysical and rock mechanical properties. An integrated reservoir simulation and geomechanical modeling are then performed to estimate the well injectivity, storage capacity, surface displacement, integrity of reservoir and caprock, and fault stability. The presented workflow demonstrates how the stacked storage approach helps with large-scale geologic carbon sequestration within structurally complex reservoirs.

Introduction

Geological carbon storage is seen as a promising approach to reducing climate change impacts by storing greenhouse gases, typically carbon dioxide (CO_2), under the subsurface (Bickle, 2009). Current commercial-scale CO_2 storage projects can inject millions of metric tons of CO_2 per year into geological porous media like saline aquifers, depleted oil and gas reservoirs, and unmineable coal seams (Aminu et al., 2017), where their caprock and surrounding faults can provide the desired structural trapping. On the other hand, whether the injected CO_2 can be stored long-termly under the subsurface also requires a reliable assessment of geomechanical risks at the storage site (Rutqvist, 2012). For example, subsurface injection

of CO_2 can influence the in-situ effective stress state due to continuous pore pressure increment, which will reduce the geomechanical integrity of caprock and reactivate the existing faults when a critical pressure change is reached. In the worst conditions, the injected CO_2 may leak through the induced pathway and into the freshwater formations and surface (Song et al., 2023). Therefore, the geomechanical effects resulting from the injection operations should be evaluated to ensure the sealing integrity of injected CO_2.

The goal of this study is to investigate the geomechanical effects during CO_2 injection for a commercial-scale geological storage complex named Wyoming CarbonSAFE project at the Dry Fork station. This project aims to safely store more than 50 million metric tons of CO_2 over 30 years in three stacked saline aquifers in the Powder River Basin (Jiao et al., 2022). Two stratigraphic wells (PRB#1 and PRB#2) have been drilled to collect site-specific data. A coupled reservoir-geomechanical simulation is conducted in this study to evaluate the injection-induced stress and strain changes, surface displacement, integrity of reservoir and caprock, and fault stabilities.

Methods

The following introduces the geological settings at the selected storage site, the process of constructing one-dimensional and three-dimensional mechanical earth models, and the setup for both reservoir and geomechanical simulations.

(1) Geological Model and Reservoir Simulation

Age		Formation/Member	
Recent		alluvium and stream terraces	
Paleocene		Fort Union Formation	
		Lance Formation	
		Fox Hills Sandstone	
Upper Cretaceous		Pierre (Lewis) Shale	
		Niobrara Formation	
		Carlile Shale	
		Belle Fourche Shale	
		Mowry Shale	Seal
		Muddy Sandstone	
Lower Cretaceous		Skull Creek Shale	Seal
		Fall River (Dakota) Formation	Seal
	Fuson Shale		
		Lakota Formation	Reservoir
		Morrison Formation	
Upper Jurassic	Upper Sundance	Redwater Shale member	Seal
	Lower Sundance	Hulett Sandstone member	Reservoir
		Stockade Beaver Shale member	
		Canyon Springs Sandstone member	
Middle Jurassic		Gypsum Spring Formation	
Triassic		Spearfish Formation	
Permian	Goose Egg Formation	Ervay Salt member	
		Minnekahta Limestone	
		Opeche Formation	Seal
Pennsylvanian		Minnelusa Formation	Reservoir
Mississippian		Madison Limestone	

Figure 1. The stratigraphic chart of the Dry Fork geological CO_2 storage site, showing the targeted reservoirs and their major confining layers.

The selected storage site is in Gillette of Wyoming State, which is located in the center of the Powder River Basin. As shown in Figure 1, three reservoir and sealing formation pairs are identified in the previous pre-feasibility study. In the order of decreasing depth, these combinations include Upper Minnelusa formation sealed by Opeche shale and Goose Egg formation, Hulett sandstone sealed by Upper Sundance formation, and Lakota sandstone sealed by Fuson shale, Skull Creek shale and Mowry shale (Quillinan and Coddington, 2019).

The geological model consists of 6 stratigraphic zones from the Upper Minnelusa formation to the Skull Creek shale, with the Upper Minnelusa formation (primary target reservoir) divided into 8 sub-zones. Three basement faults are identified with a predominant direction from northeast to southwest and all of them are confined in the lowermost Upper Minnelusa formation. The reservoir model covers an area of 24 miles by 24 miles and hexahedral grids are generated along the strike direction of the basement faults. The average horizontal dimension is 1,000 ft by 1,000 ft, while the vertical dimension ranges from 10 to 20 ft for reservoirs and from 20 to 50 ft for non-reservoir units, which results in a total of 1,952,544 grid blocks (172 ×172 ×66). The reservoir porosity is generated with Sequential Gaussian Simulation and is constrained by a lithology map produced from Sequential Indicator Simulation. The correlations between porosity and permeability, obtained from routine core analysis, are used to convert the porosity to permeability with its respective facies and formation. The relative permeability curves are measured through the core flooding test by mimicking the drainage process of CO_2 displacing brine solutions (Yu et al., 2023). A pore volume multiplier is applied along the reservoir boundary to simulate the open boundary condition. Based on the interpretation of seismic data, all basement faults are assumed to be non-sealing by setting up the transmissibility multiplier as one.

The designed simulation scenarios intend to inject CO_2 into all three stacked reservoirs simultaneously. Specifically, five well pads are placed according to surface conditions including land ownership, ease of road accessibility and subsurface petrophysical qualities. Each well pad consists of three vertical wells with each well responsible for injection into one target formation. All wells are perforated through the whole reservoir section for maximum injectivity. A group control model is applied to constrain the injection process. Specifically, the maximum bottom hole pressure is calculated based on the fracture gradient, measured through the step rate test, and a safety factor of 90%, while the maximum wellhead pressure is set at 2,400 psi for all wells. The maximum surface rate is constrained by a regional experiential value of half a million tons per year. A 30-year CO_2 injection period is simulated with another 30-year shut-in period to monitor how injected CO_2 equilibrates with surrounding brines. The simulated pressure change, due to CO_2 injection, is then integrated into the geomechanical simulation to evaluate the evolution of the in-situ stress state.

(2) One-Dimensional Mechanical Earth Model

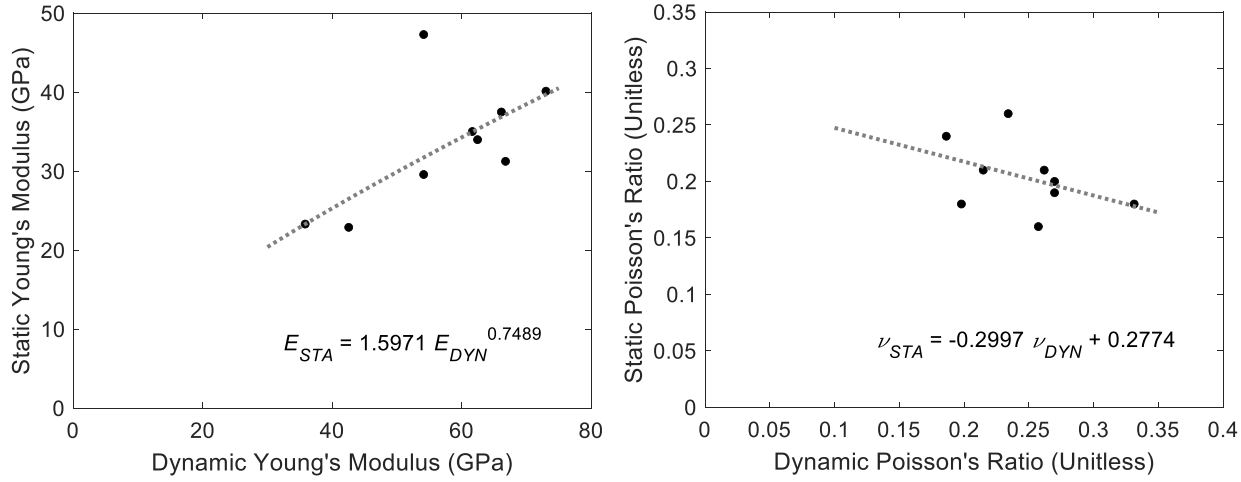

Figure 2. Correlations between static and dynamic elastic properties for (left) Young's modulus and (right) Poisson's ratio based on core data from the triaxial test.

One-dimensional mechanical earth model (1D-MEM) numerically represents the variation of rock mechanical properties and in-situ stress state along a wellbore, which has been built for all wells with available data. The dynamic rock elastic properties, including Young's modulus (E_{DYN}) and Poisson's ratio (υ_{DYN}), are derived from the acoustic log and density log based on empirical correlations. The density log is

extrapolated when it is partially missing or does not start from the surface. When the well logs for shear slowness and density are completely unavailable, the correlations developed by Castagna et al. (2012) and Gardner et al. (2012) are used to estimate them, correspondingly, based on the available compressional slowness log. The static counterparts, including E_{STA} and υ_{STA}, are obtained by fitting equations, $E_{STA} = A \times E_{DYN}{}^{B}$ and $\upsilon_{STA} = C \times \upsilon_{DYN} + D$, to the core data measured from the triaxial test, where A, B, C and D are fitting parameters. The fitted correlations are shown in Figure 2.

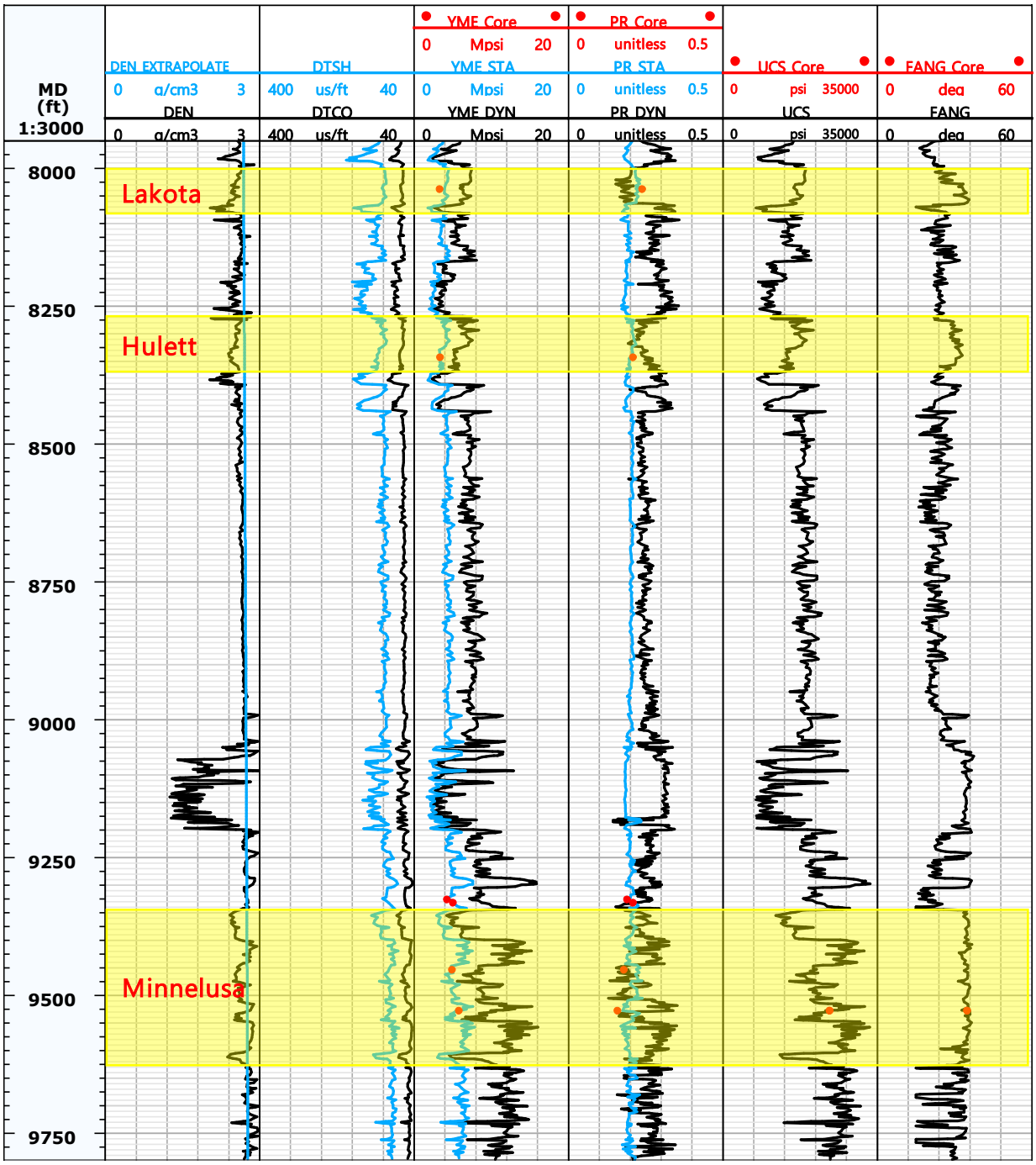

Figure 3. The profile of estimated static and dynamic elastic properties and rock strength parameters from 7950 to 9800 ft (MD).

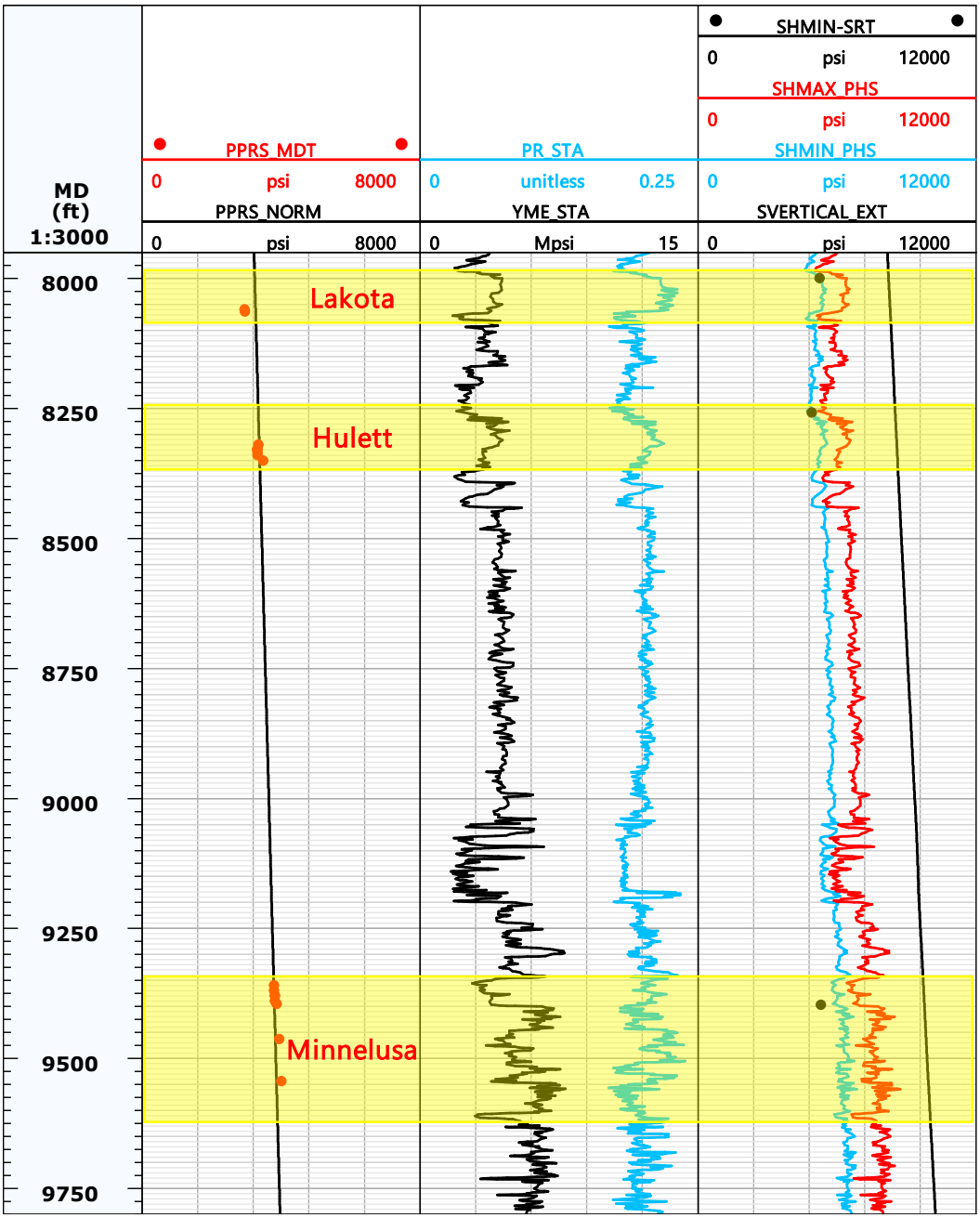

Figure 4. The profile of estimated vertical stress, minimum horizontal stress, and maximum horizontal stress from 7950 to 9800 ft (MD).

The unconfined compressive strength (UCS or C_0) is estimated with the Plumb generic static Young's modulus correlation (Plumb, 1994) by calibrating to the core data: $C_0 = 4.424E_{STA}$. Similarly, a linear transformation approach is used to estimate friction angle by mapping it to the gamma-ray log. The linear conversion equation is defined with two specified points, where each point includes the corresponding friction angle for a measured gamma-ray value. A cutoff process is also applied to constrain the minimum and maximum value of the friction angle. The estimated static elastic properties and rock strength parameters for PRB#1 well are shown in Figure 3.

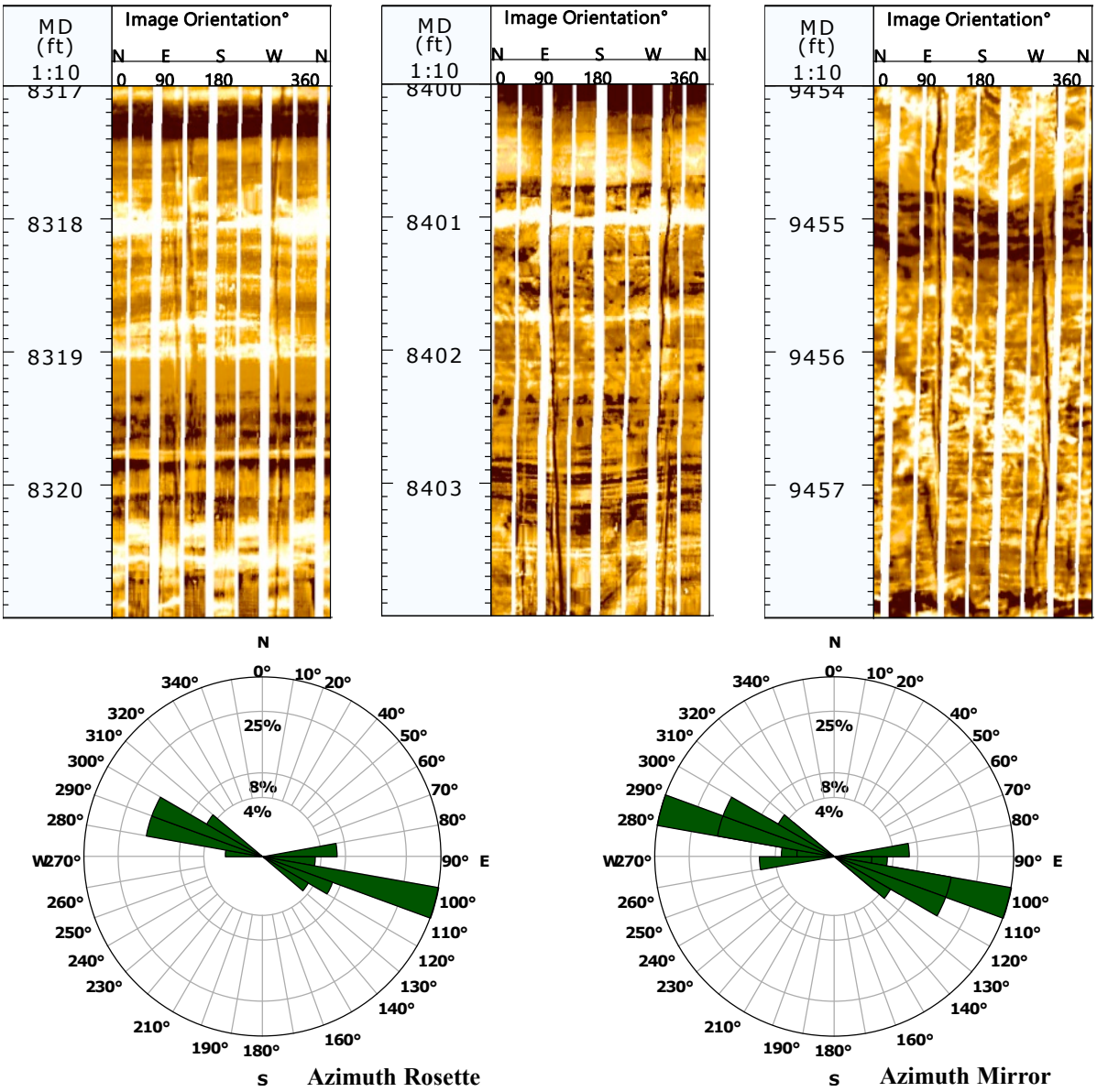

Figure 5. (Top) three examples of drilling-induced fractures identified from the image log of PRB#1 well, (Bottom) rose diagram showing the azimuth of all identified drilling-induced fractures in PRB#1 well.

The in-situ stress state under the subsurface can be fully described with three principal stresses, including vertical stress (S_v) and minimum/maximum principal horizontal stresses (S_{hmin}/S_{Hmax}), where their directions are orthogonal to each other. The vertical stress, exerted by the overburden, can be estimated by integrating over the density log. The variation of both horizontal stresses is contributed by the movement of tectonic plates. In our case, the poroelastic horizontal strain model is used to estimate them:

$$\sigma_{hmin} = \frac{\upsilon}{1-\upsilon}\left(S_V - \alpha P_p\right) + \alpha P_p + \frac{\upsilon E}{1-\upsilon^2}\varepsilon_{Hmax} + \frac{E}{1-\upsilon^2}\varepsilon_{hmin}, \quad (1)$$

$$\sigma_{Hmax} = \frac{\upsilon}{1-\upsilon}\left(S_V - \alpha P_p\right) + \alpha P_p + \frac{\upsilon E}{1-\upsilon^2}\varepsilon_{hmin} + \frac{E}{1-\upsilon^2}\varepsilon_{Hmax}, \quad (2)$$

where α is the Biot coefficient assumed to be a constant of one, P_p is the pore pressure estimated based on Eaton's method (Eaton, 1976) and calibrated with the data measured with the MDT tool, ε_{hmin} and ε_{Hmax} are two horizontal strains along the direction of minimum horizontal stress and maximum horizontal stress and are calibrated against the field measurements of minimum horizontal stress through the step rate test. The estimated pore pressure and three principal stress components for PRB#1 well are shown in Figure 4. It should be noted that the measured fracture gradient for the Upper Minnelusa formation is not as accurate as those for the Lakota and Hulett formations. As shown in Figure 4, it is thus not used for calibration and exhibits a relatively large shift from the calculated minimum horizontal stress at the Upper Minnelusa formation.

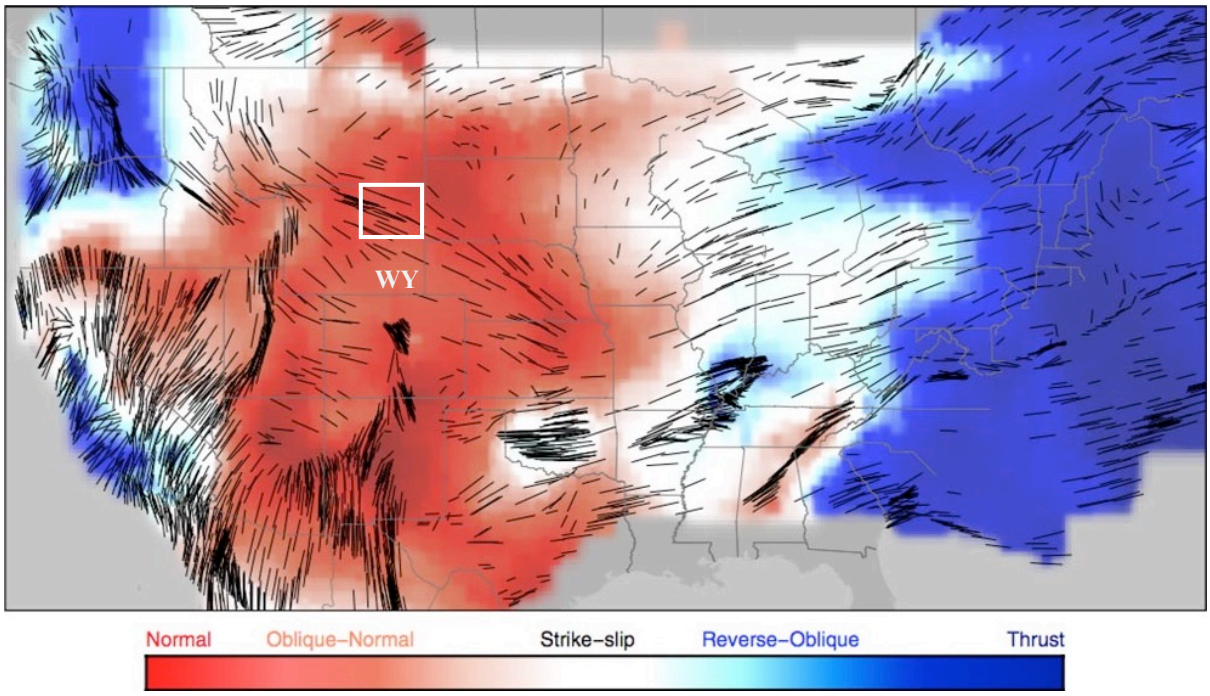

Figure 6. Direction of maximum horizontal stress at the study site indicated by the US stress map (Levandowski et al., 2018), which shows the stress regime and orientation of inferred maximum horizontal stress across the United States. The white square indicates the location of the study site.

(3) Three-Dimensional Mechanical Earth Model

As shown in Figure 7, the geomechanical grid is constructed by extending the reservoir model up to the ground surface, down to a surface at a depth of roughly 14,000 ft, and laterally by three times to model overburden, underburden and sideburden and to mitigate the boundary effects over the domain of interest. A geometric factor of 1.3 is used to constrain the size of neighboring grids in the horizontal direction to reduce the computational cost. The thickness ratio for two adjacent layers in both overburden and underburden ranges from 1.1 to 1.2. The final geomechanical grid consists of 5,541,316 cells (214×214×121). 1D-MEM is constructed for roughly 200 wells in the study area and then upscaled to the 3D geomechanical grid. Due to limited triaxial core data, it should be noted that the correlations derived from PRB#1 well are used to calculate the rock mechanical properties for other wells. The three-dimensional mechanical earth model (3D-MEM) is constructed by interpolating all the 1D-MEMs based on Sequential Gaussian Simulation. Figure 8 shows the simulated spatial distribution of static Young's modulus in the reservoir grid, which demonstrates the high heterogeneity of the subsurface at the study area. The mechanical properties of all basement faults are set up based on the works from Ouellet et al. (2011).

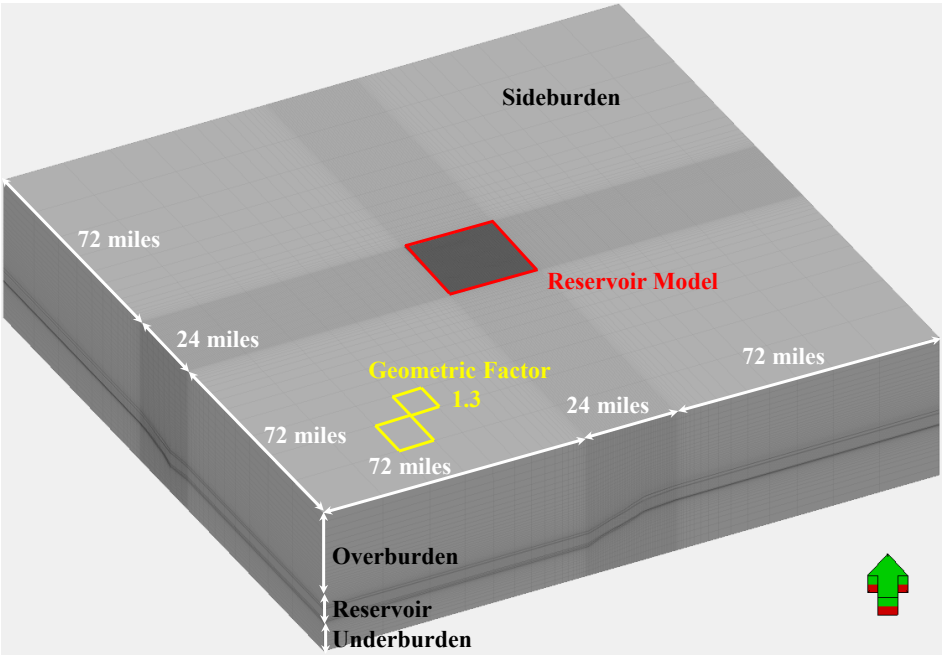

Figure 7. 3D geomechanical grid extended from the reservoir model by adding the overburden, underburden and sideburden.

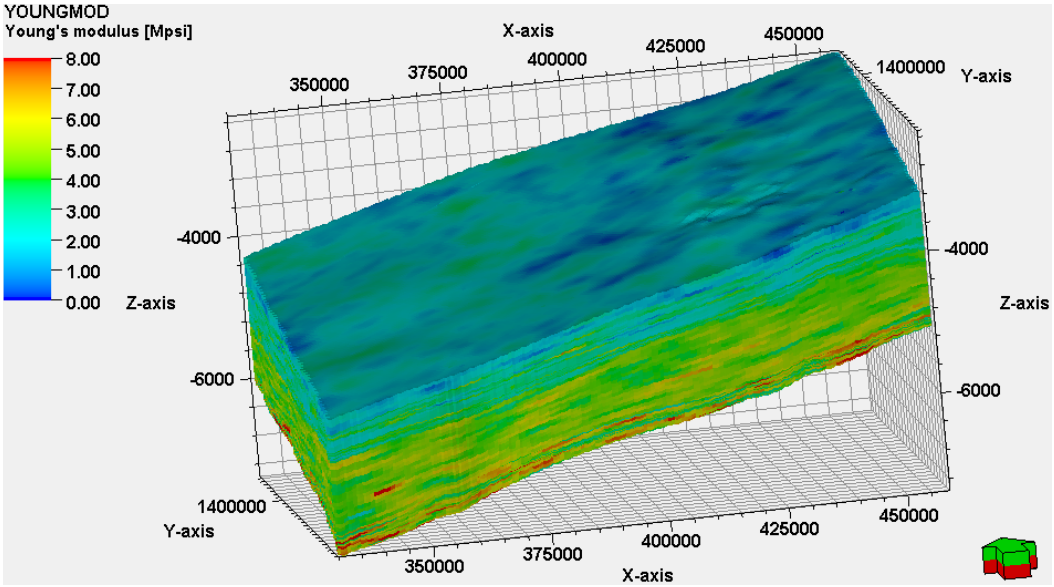

Figure 8. Distribution of static Young's modulus modeled by interpolating 1D-MEMs with Sequential Gaussian Simulation. Vertical resolution is enlarged by 15 times for better demonstration.

(4) Model Setup

This study uses both Eclipse-300 and Visage simulators to run a coupled fluid flow and geomechanical simulation. The one-way coupling approach is used to calculate the change of stress and strain resulting from pore pressure increment due to CO_2 injection (Prevost, 2013). The two horizontal strains, ε_{hmin} and ε_{Hmax}, derived from the previous poroelastic horizontal strain model, are used to set up the strain boundary condition for stress initialization with the estimated regional stress state. The ground surface is allowed to

move freely for estimating its displacement caused by CO_2 injection. The Mohr-Coulomb failure criteria are used to determine the integrity of the reservoir and caprock and the stability of all basement faults. In particular, the faults are assumed to be cohesionless where the Mohr-Coulomb failure envelope will go through the origin.

Results

At the end of the 30-year injection period, a total amount of 84 million metric tons of CO_2 can be stored in this stacked reservoir-caprock system, where the Upper Minnelusa formation and the Hulett sandstone contribute to 56.1% and 29.6% of the total injection respectively. Figure 9 shows the well pad locations and the CO_2 plume at the end of the 30-year shut-in period at which the largest CO_2 plume size can be expected with the achieved pressure equilibrium. The Area of Review (AoR) calculated based on the EPA approach (United States Environmental Protection Agency, 2015) for each targeted reservoir is also shown in Figure 9.

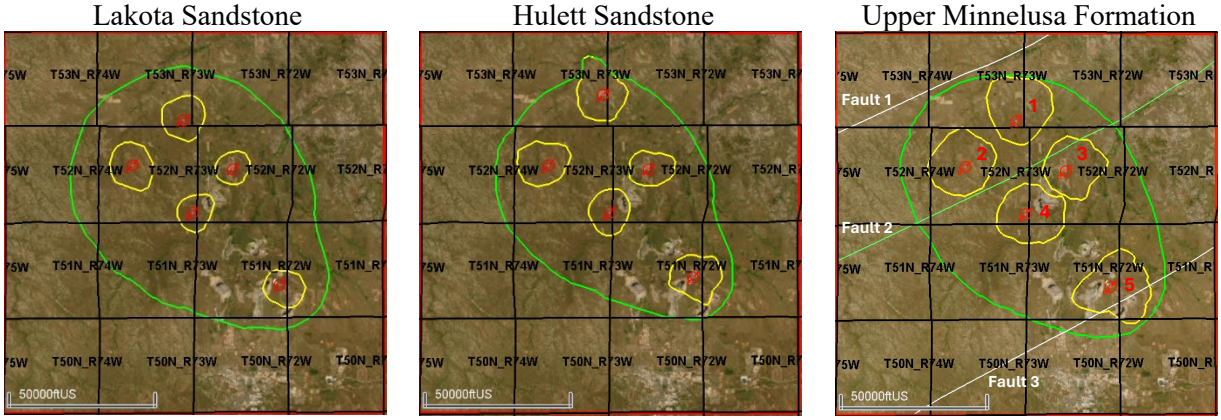

Figure 9. CO_2 plume (yellow), AoR (green), and location of well pads (red) for each targeted reservoir. The strikes of all basement faults in the Upper Minnelusa formation are also shown.

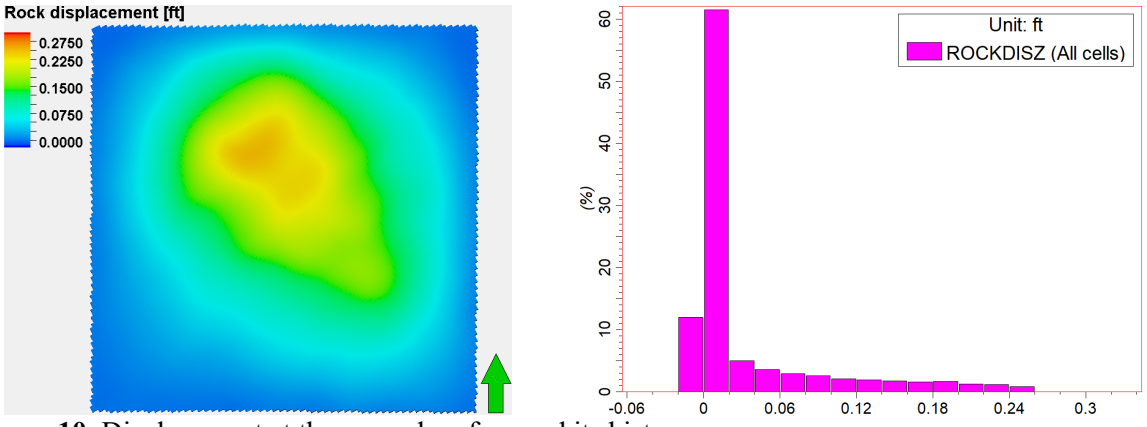

Figure 10. Displacement at the ground surface and its histogram.

The maximum pore pressure increment is observed near the injection well at the Lakota sandstone with a value of roughly 1,100 psi. The induced pressure changes are used to update the stress and strain state in the subsurface. Figure 10 shows the displacement of the ground surface and its histogram. It can be observed that the maximum surface uplift is 0.26 ft (or 7.92 cm) at the location near the injection wells. The displacements in most of the areas (roughly 60%) are less than 0.02 ft (or 0.61 cm). Very few grid cells, especially those along the model boundary, exhibit negative displacements due to the applied pore volume multiplier, which can be optimized to some extent to balance the aim of modeling the open boundary condition and reduction of induced displacement artifacts.

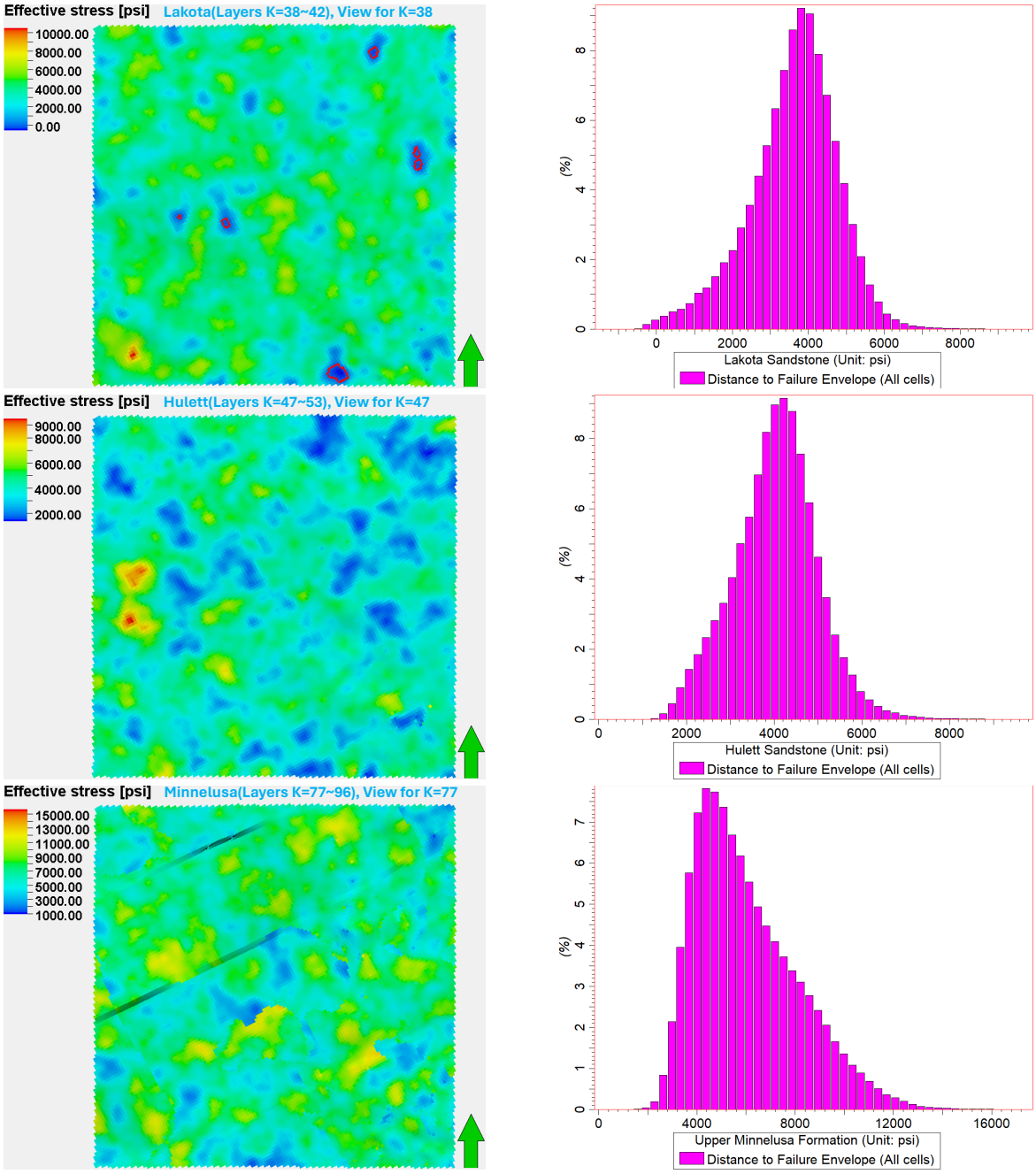

Figure 11. Integrity analysis based on Mohr-Coulomb failure criteria for each targeted reservoir. The distance between Mohr's circle and the failure envelope is shown in the left figures, while its histogram is in the right figures. The red polygons indicate where shear failure happens.

The Mohr-Coulomb failure criteria are used to evaluate the integrity of each targeted reservoir. The maximum pressure increment is achieved at the end of the injection period, after which injected CO_2 equilibrates with brines and the pore pressure continuously decreases. Thus the reservoir at this time is most likely to fail as the potential largest reduction of effective stress appears. The specific stress state is then represented by the Mohr's circle and the distance between it and the failure envelope is calculated for each grid cell, which is shown in Figure 11. It can be observed that only a very small part of grid cells for Lakota sandstone fail while the other two targeted reservoirs preserve their integrity. It's worth noting that the

reservoir heterogeneity significantly influences the assessment of the reservoir integrity during CO_2 injection.

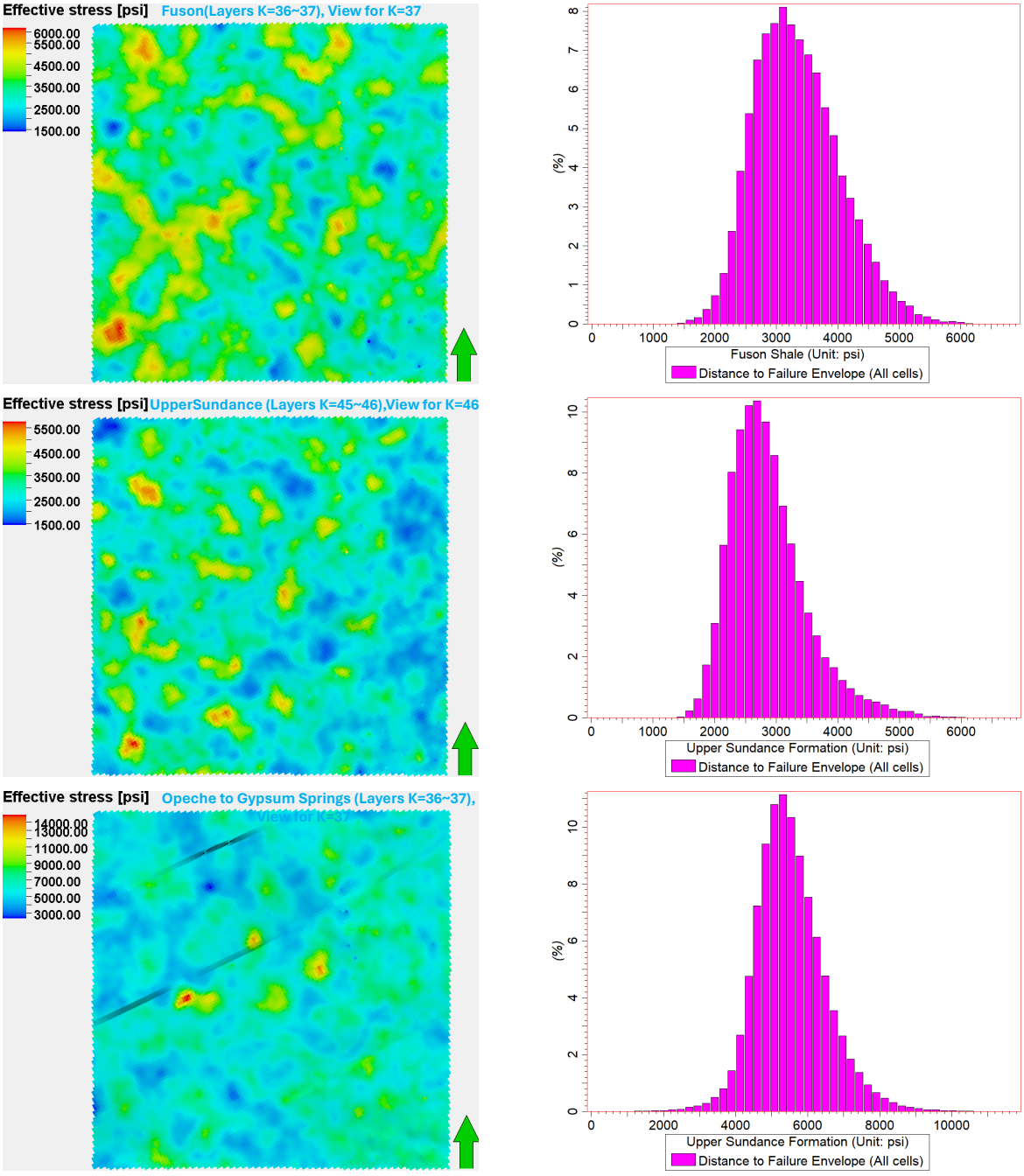

Figure 12. Integrity analysis based on Mohr-Coulomb failure criteria for caprock corresponding to each targeted reservoir.

The same approach is used to evaluate the integrity of all caprocks. As shown in Figure 12, at the end of the injection the distances between Mohr's circle and failure envelope for all gird cells remain positive, thus the integrity of caprock is also preserved.

The Mohr-Coulomb failure criteria are also used to assess the stability of all basement faults with the assumption of cohesionless faults. As shown in Figure 13, the grid cells, touching with or going across the

failure envelope, are labeled with red color. Most of the grid cells for each fault remain stable during CO_2 injection. It is also found that the rock mechanical properties or the reservoir heterogeneities play a major role in determining the fault stability as a clear correspondence between the failure indicator map and the spatial distribution of rock mechanical properties can be observed, which indicates there is potential room for pore pressure increment.

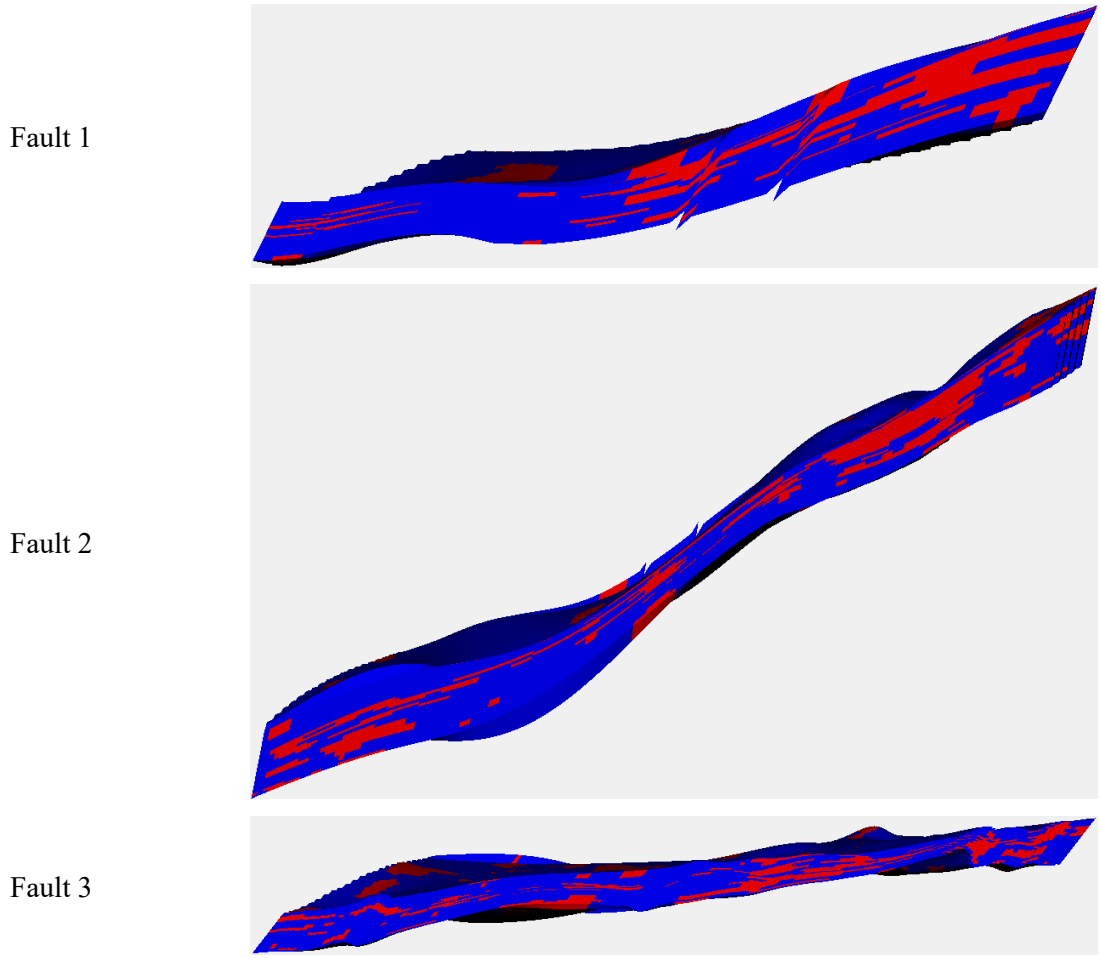

Figure 13. Fault stability indicated by different colors (blue: stable, red: unstable). Vertical resolution is enlarged by 50 times for better demonstration.

Discussion

The available 3D seismic data only covers an area of 3 miles by 3 miles, which is much smaller compared to the size of the dynamic model. Therefore, uncertainties do exist in the interpretation of all basement faults. Another scenario assuming sealing faults is also conducted to investigate its potential influence on the stress and strain change in the subsurface. Figure 14 compares the ground surface displacement for different scenarios, which indicates that sealing faults retard the pressure dissipation and a larger surface uplift is observed, demonstrated by the histogram. On the other hand, it can be observed that some grid cells in faults 2 and 3 become unstable in the sealing fault scenario, as indicated by the red color in Figure 15. All of them are close to well pads 2, 4 and 5, which have larger injectivities compared to the other two well pads.

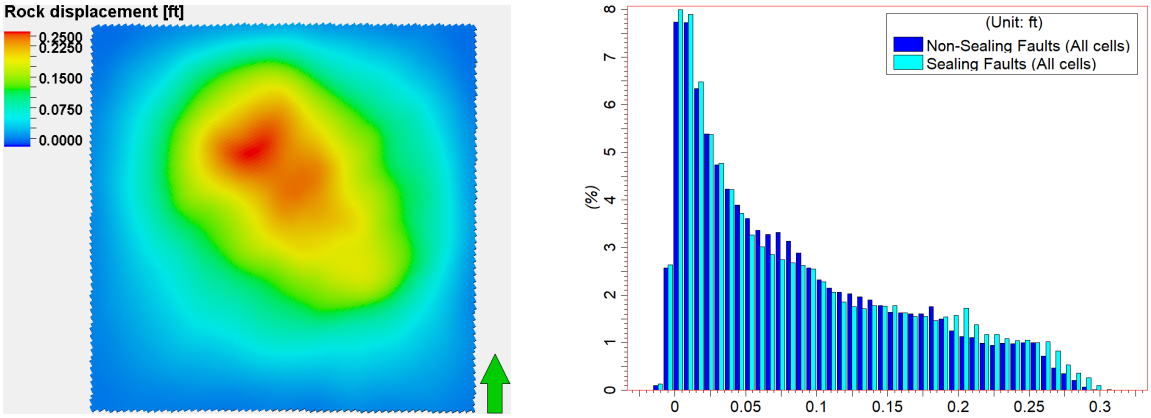

Figure 14. Comparison of surface displacements simulated based on different scenarios with sealing and non-sealing faults.

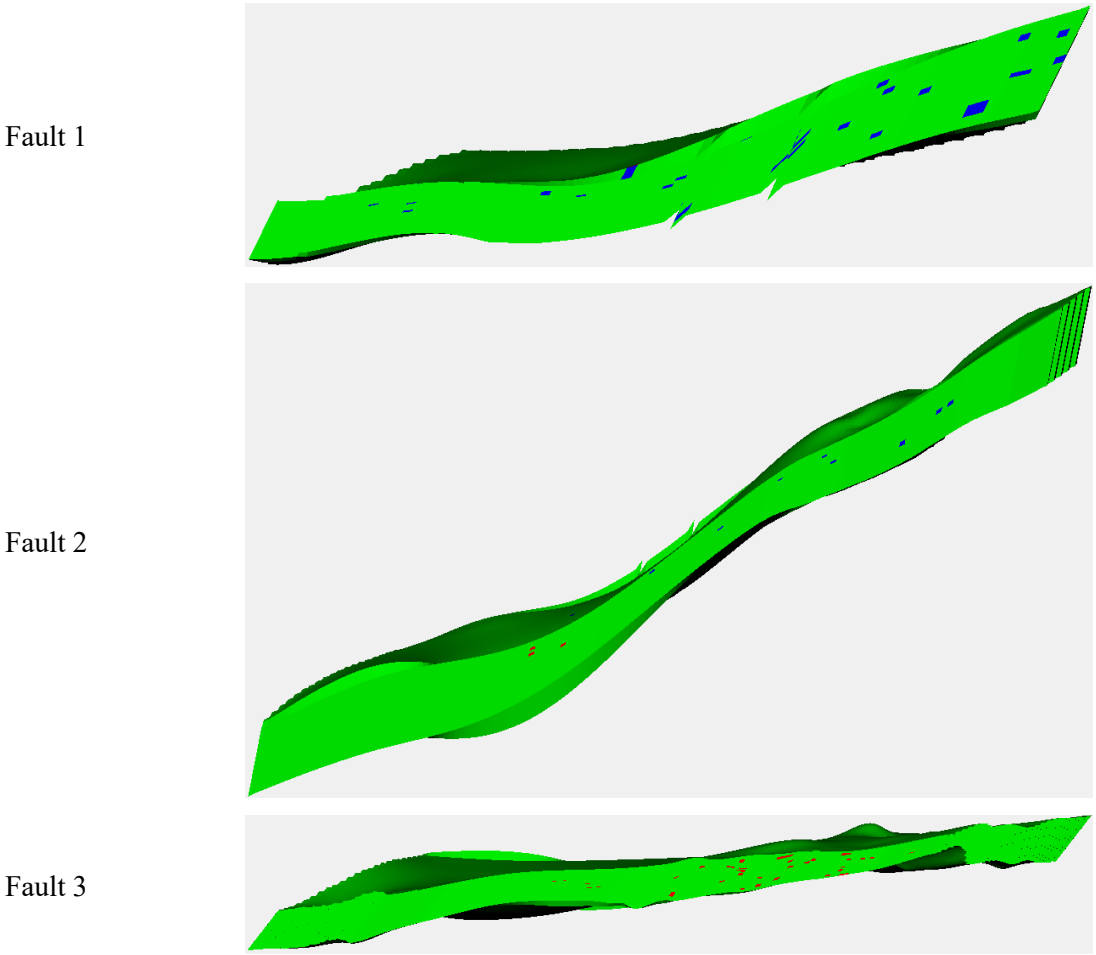

Figure 15. Comparison of fault stability simulated based on different scenarios with sealing and non-sealing faults. The red color indicates the newly added unstable grid cells for the scenario of sealing faults, while the blue color indicates where the originally unstable grid cells are converted to stable for the same scenario.

Conclusions

To assess the geomechanical risks associated with geological CO_2 storage at the Wyoming CarbonSAFE Dry Fork Station site, a coupled fluid flow and geomechanical simulation is conducted based on the one-way coupling approach. Multiple 1D-MEMs are constructed with well-log data to estimate rock mechanical properties and strength parameters and calibrated against the core data. 3D-MEM is then constructed through geostatistical modeling methods. Regional stress state and initial conditions are calibrated against field measurements and other field observations recorded in the literature. The results indicate that the integrity of both reservoir and caprock are preserved, faults show the potential to bear higher pore pressure increment and a limited surface uplift can be expected during CO_2 injection.

Acknowledgements

The authors would like to thank the Department of Energy for funding through the grants DE-FE0031624 and DE-FE0031891.

References

Aminu, M. D., S. A. Nabavi, C. A. Rochelle, and V. Manovic, 2017, A review of developments in carbon dioxide storage: Applied Energy, v. 208, p. 1389–1419, doi:10.1016/J.APENERGY.2017.09.015.

Bickle, M. J., 2009, Geological carbon storage: Nature Geoscience 2009 2:12, v. 2, no. 12, p. 815–818, doi:10.1038/ngeo687.

Castagna, J. P., M. L. Batzle, and R. L. Eastwood, 2012, Relationships between compressional-wave and shear-wave velocities in clastic silicate rocks: https://doi.org/10.1190/1.1441933, v. 50, no. 4, p. 571–581, doi:10.1190/1.1441933.

Eaton, B. A., 1976, Graphical method predicts geopressures worldwide: World Oil; (United States), v. 183:1.

Gardner, G. H. F., L. W. Gardner, and A. R. Gregory, 2012, FORMATION VELOCITY AND DENSITY—THE DIAGNOSTIC BASICS FOR STRATIGRAPHIC TRAPS: https://doi.org/10.1190/1.1440465, v. 39, no. 6, p. 770–780, doi:10.1190/1.1440465.

Jiao, Z., M. Johnson, F. McLaughlin, T. Bai, Y. Yu, and Y. Ganshin, 2022, Challenges for commercial-scale CCS in the saline aquifer: A case study — Wyoming CarbonSAFE DF project, Powder River Basin, Wyoming: SEG Technical Program Expanded Abstracts, v. 2022- August, p. 454–456, doi:10.1190/IMAGE2022-3736466.1.

Levandowski, W., R. B. Herrmann, R. Briggs, O. Boyd, and R. Gold, 2018, An updated stress map of the continental United States reveals heterogeneous intraplate stress: Nature Geoscience 2018 11:6, v. 11, no. 6, p. 433–437, doi:10.1038/s41561-018-0120-x.

Ouellet, A., T. Bérard, J. Desroches, P. Frykman, P. Welsh, J. Minton, Y. Pamukcu, S. Hurter, and C. Schmidt-Hattenberger, 2011, Reservoir geomechanics for assessing containment in CO2 storage: A case study at Ketzin, Germany: Energy Procedia, v. 4, p. 3298–3305, doi:10.1016/J.EGYPRO.2011.02.250.

Plumb, R. A., 1994, Influence of Composition and Texture on the Failure Properties of Clastic Rocks: Society of Petroleum Engineers - Rock Mechanics in Petroleum Engineering 1994, p. 13–20, doi:10.2118/28022-MS.

Prevost, J. H., 2013, One-Way versus Two-Way Coupling in Reservoir-Geomechanical Models: Poromechanics V - Proceedings of the 5th Biot Conference on Poromechanics, p. 517–526, doi:10.1061/9780784412992.061.

Quillinan, S., and K. Coddington, 2019, Integrated Commercial Carbon Capture and Storage (CCS) Prefeasibility Study at Dry Fork Station, Wyoming: doi:10.2172/1557442.

Rutqvist, J., 2012, The Geomechanics of CO2 Storage in Deep Sedimentary Formations: Geotechnical and Geological Engineering 2012 30:3, v. 30, no. 3, p. 525–551, doi:10.1007/S10706-011-9491-0.

Song, Y., S. Jun, Y. Na, K. Kim, Y. Jang, and J. Wang, 2023, Geomechanical challenges during geological CO2 storage: A review: Chemical Engineering Journal, v. 456, p. 140968, doi:10.1016/J.CEJ.2022.140968.

United States Environmental Protection Agency, 2015, Underground Injection Control (UIC) Program Class VI Well Area of Review Evaluation and Corrective Action Guidance.

Yu, Y., S. Farzana, C. Nye, D. Bagdonas, P. R. Waghmare, Z. Jiao, and J. F. McLaughlin, 2023, Wettability variation and its impact on CO2 storage capacity at the Wyoming CarbonSAFE storage hub: An experimental approach: Fuel, v. 344, p. 128111, doi:10.1016/J.FUEL.2023.128111.